JOURNAL OF Materials CHEMISTRY

Defect chemistry and surface properties of $LaCoO_3$

Mark S. D. Read,[a] M. Saiful Islam,*[a] Graeme W. Watson,[b] Frank King[c] and Fred E. Hancock[c]

[a]*Department of Chemistry, University of Surrey, Guildford, UK GU2 5XH. E-mail: m.islam@surrey.ac.uk*
[b]*Department of Chemistry, Trinity College, Dublin 2, Ireland*
[c]*Synetix, P.O. Box 1, Billingham, Cleveland, UK TS23 1LB*

Received 17th March 2000, Accepted 7th August 2000
First published as an Advanced Article on the web 6th September 2000

Atomistic computer simulation techniques are used to investigate the surface properties and defect chemistry of the $LaCoO_3$ perovskite. The theoretical techniques are based upon efficient energy minimisation routines, a 'two-region' strategy and the Mott–Littleton methodology for the accurate modelling of surface and bulk defects. Sr and Ca dopants are calculated to be the most soluble of the alkaline earth metals, in accord with observation. Charge compensation is predicted to occur *via* oxygen ion vacancies which are believed to be key sites with regard to catalytic activity. Relaxed surface energies are calculated for the low index surfaces and the order of stability is found to be $\{110\} > \{100\} > \{111\}$. The equilibrium morphology of $LaCoO_3$ is predicted from the surface energies, in which the {110} surface is calculated to dominate in the absence of impurities or surface irregularities, with a lesser contribution from the {100} surface. The surface defect energies are generally lower than in the bulk crystal implying that the dopants and oxygen vacancies will segregate to the surfaces, thus enhancing their catalytic and electrochemical activity.

1 Introduction

Mixed-metal oxides with the perovskite structure (Fig. 1) and overall stoichiometry $LaBO_3$ (B = Al, Cr, Mn, Fe or Co) have received considerable attention as efficient heterogeneous catalysts,[1–22] as electrode materials for solid oxide fuel cells[23–33] and other electrochemical applications. More specifically, these oxides are catalytically active in the oxidation of CO and reduction of NO_x for application in auto-exhaust treatment.[1,2,11–14,34] Other catalytic reactions include the oxidative coupling of methane to form C_2 hydrocarbons,[6–10] a process of much importance in utilising the abundant reserves of natural gas.

Recent interest relates to the fact that nuisance odours, often containing sulfur species, are a high profile emission in many types of process industry (*e.g.* food processing, sewage treatment works). Oxidation of these sulfur species is usually easy and their removal from the gas stream by absorption into a dilute aqueous oxidising agent can be effective in de-odourising the air. However, it is possible to increase the oxidative reaction rate with a catalyst and this enhancement can be such that for most applications the catalytic process is the commercial solution. It is believed that $LaCoO_3$ based materials have an important role in odour abatement catalysis.

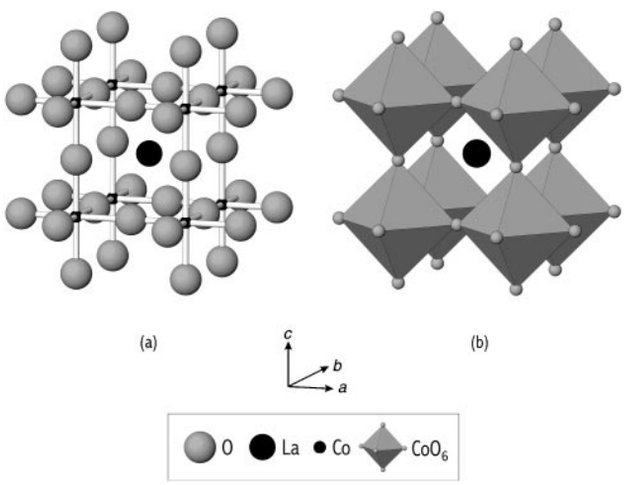

Fig. 1 Crystal structure of $LaCoO_3$ showing (a) atomic positions of the unit cell and (b) structure depicting CoO_6 corner-sharing octahedra, with the A cations occupying the central interstice, and the B cations residing in the centre of the octahedra.

The partial substitution of the La(III) site with cations of lower valency (*e.g.* Sr(II)) has been shown to greatly alter the catalytic and electrical characteristics of these materials. This type of acceptor doping leads to charge compensation by an increase in the valence of the B site transition metal (as in $LaMnO_3$) and/or the formation of oxygen vacancies. Clearly, the role of defects and dopants, as well as the nature of the redox reactions to create electronic (hole) species, are crucial to the fundamental understanding of the behaviour of the $LaBO_3$ materials.

As an example of studies on nuisance odours or volatile organic compounds, the relative activities of a number of catalysts in the decomposition of *o*-nitrophenol and sodium benzoate by peroxide were investigated *via* the amount of organic material that was removed.[35] $LaCo_{0.5}Cu_{0.5}O_3$, $LaCo_{0.8}Cu_{0.2}O_3$, $La_{0.8}Sr_{0.2}CoO_3$ and $La_{0.8}Sr_{0.2}Co_{0.5}Cu_{0.5}O_3$ were compared with a nickel catalyst and a blank.[35] All catalysts were found to have the same percentage conversion rates (within a range of about 10%) for given flow rates, temperature and peroxide concentrations. However, during these tests the catalysed reactions were observed to produce significant amounts of oxygen, from the breakdown of hydrogen peroxide.

Clearly it would be detrimental to destroy the H_2O_2 which is used to oxidise the organic compounds. Since the various catalysts yielded similar activities towards the decomposition of organic materials, the relationship between catalyst formulation of a range of perovskite-type oxides and the breakdown of H_2O_2 was subsequently examined. The general trend from such data is that strontium doping increases activity up to an apparent maximum, and the addition of copper

 DOI: 10.1039/b002168g

conversely decreases the activity. Additionally, the cubic perovskite structure ($LaBO_3$) is more active than the layered perovskite-like structure (La_2BO_4).

Some studies propose that strontium addition provides either Cu(III) or Co(IV), for a given oxygen content hence increasing the ability of the lattice to decompose hydrogen peroxide. However, it has also been proposed that oxygen vacancies play a key role in the decomposition of H_2O_2. Indeed, considerable speculation has centred on the role of oxygen species or defects in the partial and complete oxidation of various reducing compounds (*e.g.* alkanes, alkenes, aromatics and ammonia).[5] The aims of this modelling study, therefore, are to demonstrate how a valid atomistic model of $LaCoO_3$ can be used to examine the defect and surface structures, and to provide further insight into the catalytic behaviour.

2 Simulation methodology

The atomistic simulations presented here use the same methodology for the treatment of perfect and defective bulk lattices as employed in our previous studies of solid catalysts (*e.g.* La_2NiO_4,[36] La_2O_3[37] and $LaMO_3$[38]) and are embodied within the GULP[39] code. The computer code METADISE[40] (Minimum Energy Techniques Applied to Dislocation Interface and Surface Energies) using the approach described by Tasker,[41] was used to perform the simulations on the surfaces of $LaCoO_3$.

As these techniques have been discussed extensively in earlier studies,[36,42] only the key aspects for the treatment of surfaces will be outlined here. The simulations are based on the Born model of ionic solids, in which the long-range terms are evaluated for the surface simulations by a plane-by-plane summation due to Parry[43] and the Ewald procedure[44] (which is routinely used for bulk simulations). Because of the two-dimensional periodicity of the surface calculation, we eliminate the need for large voids between blocks which is required in the alternate slab methodology. The Coulombic interaction is supplemented with a Buckingham potential to account for the short-range repulsion between neighbouring electron charge clouds and the van der Waals attraction. The short-range potential is given by

$$V = A_{ij}\exp\left(-\frac{r_{ij}}{\rho_{ij}}\right) - \frac{C_{ij}}{r_{ij}^6} \quad (1)$$

where the ions i and j are separated by a distance r_{ij} and A_{ij}, ρ_{ij} and C_{ij} are variable parameters fitted to the lattice properties. The potential parameters used in this study are those employed in our previous simulations of $LaCoO_3$ (Table 1), which reproduce the observed perovskite structure to within 0.5% of the lattice parameters.[45]

The structure (and energy) of a surface were then obtained by relaxing the ions to their mechanical equilibrium positions. This was achieved *via* a two region approach in which the ion coordinates in the surface region are adjusted so that they experience zero net force, whilst those ions which are distant from the surface are kept fixed at their bulk equilibrium positions. The sizes of the surface regions were chosen to be large enough to ensure that the surface energy had converged.

The energy (γ_i) of a particular surface is calculated from the difference between the surface block and the same number of bulk ions per unit area, thus

$$\gamma_i = \left(\frac{E_{\text{surf}} - E_{\text{bulk}}}{\text{area}}\right) \quad (2)$$

As periodic boundary conditions are assumed, defects and impurities can be accommodated in the surface but only such that the net charge is zero[46] because the calculated Coulombic energy is divergent if the repeat cell is charged. This is also the case if there is a dipole in the repeat cell perpendicular to the surface.[47] As a consequence, Tasker[48] identified three types of surface cell or repeat unit. In Type I surfaces the surface cell is composed of single planes containing both cations and anions in a stoichiometric ratio and hence there can be no dipole perpendicular to the surface. Type II cells are composed of a number of distinct charge planes but are arranged such that the repeat cell has no dipole perpendicular to the surface. Type III surfaces are composed of alternately charged planes that produce a dipole perpendicular to the surface if the crystal is cut between any adjacent planes of atoms. If such surfaces are to be studied, and all the low index surfaces of $LaCoO_3$ are Type III, then the surface must be reconstructed such that the dipole is cancelled.[49] The simplest reconstruction is to remove half the surface plane making the surface layer 50% vacant, thus notionally transferring the ions to the opposite side of the crystal.

Direct comparison of surface energies with experiment is not always possible due to the paucity of reliable data. Nevertheless, the crystal morphology is one indirect measure which can be predicted from the surface energies using Wulff's theorem.[50] This is related to the earlier theorem of Gibbs[51] who proposed that the equilibrium form of a crystal should possess minimal total surface energy for a given volume, *i.e.*:

$$E_{\text{surf}} = \sum_i \gamma_i A_i = \text{minimum for constant volume} \quad (3)$$

where γ_i and A_i are the surface energy and surface area of the i^{th} crystallographic face. Wulff suggested that the shape thus defined would be such that h_i, the normal vector to the face

Table 1 Interatomic potentials for $LaCoO_3$

	Short-range parameters			Shell model[c]	
Interaction	A/eV	ρ/Å	C/eV Å^{-6}	$Y(\|e\|)$	k/eV Å^{-2}
(a) Perfect lattice					
$La^{3+}\cdots O^{2-a}$	1545.21	0.3590	0.0	−0.250	145.0
$Co^{3+}\cdots O^{2-a}$	1329.82	0.3087	0.0	2.040	196.3
$O^{2-}\cdots O^{2-b}$	22764.30	0.1490	43.0	−2.3890	42.0
(b) Dopants					
$Mg^{2+}\cdots O^{2-d}$	1428.5	0.2945	0.0	1.585	361.6
$Ca^{2+}\cdots O^{2-d}$	1090.4	0.3437	0.0	3.135	110.2
$Sr^{2+}\cdots O^{2-d}$	959.1	0.3721	0.0	3.251	71.7
$Ba^{2+}\cdots O^{2-d}$	905.7	0.3976	0.0	9.203	459.2
$Mn^{2+}\cdots O^{2-d}$	1007.4	0.3262	0.0	3.420	95.0
$Fe^{2+}\cdots O^{2-d}$	1207.6	0.3084	0.0	2.997	62.9
$Co^{2+}\cdots O^{2-d}$	1491.7	0.2951	0.0	3.503	110.5
$Cu^{2+}\cdots O^{2-b}$	3799.3	0.24273	0.0	2.000	999999.0

[a]Cherry *et al.*[45] [b]Baetzold and Islam.[74] [c]Y and k are the shell charge and spring constant respectively. [d]Lewis and Catlow.[55]

from a point within the crystal, would be proportional to the surface energy of that face, γ_i,

$$h_i = \lambda\gamma_i \quad (4)$$

where λ is a constant that is dependent on the absolute size of the crystal. This expression is only valid for crystals grown with all faces in equilibrium and does not take account of kinetic factors such as growth rate. For small crystals where rearrangement of the crystal at each stage of the growth process is possible, due to the small distances over which material has to travel, a morphology close to the equilibrium form would be expected. Thus the relative stability of a specific crystal face can be judged by its morphological importance.

Recent work[52–54] has also shown the value of these techniques in the investigation of the specific modification of crystal morphology in the presence of additives; a process of paramount importance to a wide variety of technological processes. Support for the general validity of the methodology is provided by a number of examples of calculated crystal morphologies that agree well with observation.[49,52,53]

3 Results and discussion

3.1 Dopant substitution in bulk $LaCoO_3$

The addition of dopant ions to the $LaBO_3$ oxides has been widely shown to be crucial to promoting catalytic activity[1–5,8,9,20,21,26,27] and electrochemical behaviour.[26–33] Such materials are commonly acceptor doped with low-valent cations which substitute for La. This reduction of the effective valence of the A site cations may lead to either the formation of a compensating population of oxygen vacancies or the formation of a hole on the transition metal B site as represented by the two defect equations:

$$2MO + 2La_{La}^{\times} + O_O^{\times} \rightleftharpoons 2M_{La}^{'} + V_O^{\cdot\cdot} + La_2O_{3(surf)} \quad (5)$$

$$2MO + 2La_{La}^{\times} + \frac{1}{2}O_2 \rightleftharpoons 2M_{La}^{'} + 2h^{\cdot} + La_2O_{3(surf)} \quad (6)$$

where MO signifies the dopant oxide and $M_{La}^{'}$ the dopant substitutional. In principle, hole formation could occur at the A site, although this is not possible for $LaCoO_3$ since La^{4+} is not observed. The positive holes are treated in localised terms as Co^{4+} and O^{-} small polaron species. Our studies have favoured cobalt holes over oxygen holes although we acknowledge that the question of whether such species have predominantly Co(3d) or O(2p) character remains unclear and would require the use of first-principles methods. Nevertheless, calculations of this type have a crucial role in unravelling the nature of the defect processes responsible for the redox chemistry.

The energies of these "solution" reactions (5 and 6) were evaluated by combining appropriate defect and cohesive energy terms. These calculated energies of solution for alkaline-earth dopants (Mg, Ca, Sr and Ba) are shown as a function of ionic radius for both charge compensation mechanisms in Fig. 2. The interatomic potentials for the dopant species are exactly those of the corresponding alkaline-earth metal oxides (Table 1);[55] these have also been successfully applied to similar studies of dopant substitution in the La_2NiO_4 catalyst,[36] the $LaGaO_3$ oxygen ion conductor[56,57] and the La_2O_3 methane coupling catalyst.[37]

Two main points emerge from these results. First, the most favourable mode of charge compensation is clearly the formation of oxygen vacancies. This result is particularly significant as it is believed that oxygen vacancies are key sites in the mechanism of H_2O_2 decomposition.[58] It is noted that the role of oxygen vacancy defects as active sites has also been discussed in relation to recent studies on NO decomposition over doped $LaCoO_3$.[34] Furthermore, oxygen ion vacancies are believed to play a key role in the reaction kinetics of methane combustion.[5] However, owing to the relatively low solution energies for hole formation, it is likely that Co(IV) will also be present. For air-calcined or oxygen-treated samples, the mixture ($La_{1-x}^{3+}Sr_x^{2+}Co_{1-2z}^{3+}Co_{2z}^{4+}O_{3-\frac{x}{2}+z}$) is reported to be the observed case,[59] which contains both oxygen vacancies and cation holes. It has been proposed that the Co^{3+}/Co^{4+} redox reaction and oxygen vacancies are responsible for the catalytic action of $La_{0.8}Sr_{0.2}CoO_3$ for NO decomposition.[34]

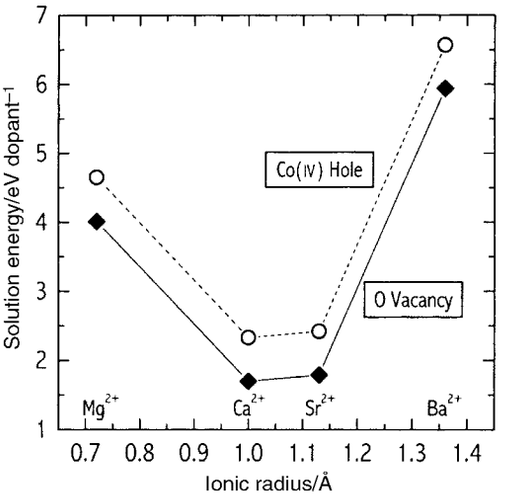

Fig. 2 Plot of solution energy as a function of ionic radius for alkaline earth metal dopants in $LaCoO_3$.

Secondly, the most favourable solution energy, and hence the highest solubility, is predicted for Ca^{2+} and Sr^{2+}. This accords with experimental work in which Sr is the most commonly used acceptor dopant leading to enhanced catalytic activity.[60] The calculations also show that a solution of Mg^{2+} and Ba^{2+} is appreciably endothermic, in line with their observed low solubility. In addition, a degree of correlation is found between the calculated solution energy and the dopant ion size with minima near the La^{3+} radius of 1.06 Å.

3.2 Sr doping of $LaCo_{1-x}M_xO_3$ (M^{3+} = Cr, Mn, Fe, Cu)

Various solid solutions of $LaCo_{1-x}M_xO_3$ (where M = Cr, Mn, Fe, Cu and $0.10 < x < 0.50$) were then simulated using the 'mean field' approach which allows the homogeneous distribution of the dopant ion. This approach, embodied within the GULP code, has been applied successfully to simulation studies of the CeO_2–ZrO_2 catalysts,[61,62] the $Li_xMn_2O_4$ spinel[63] and the $Y/Nb/ZrO_2$ oxygen ion conductor.[64] The purpose of these simulations is to establish which mode of charge compensation prevails when the Co is partially replaced with varying amounts of trivalent transition metal and examine any link with the observed catalytic performance.

Focusing on Sr as the commonly used dopant, trends are examined between the energy of Sr solution for the $LaCo_{1-x}M_xO_3$ system with charge compensation occurring *via* either Co(IV) holes or oxygen vacancies. The trend of solution energy as a function of Co replacement for the Cr and Mn dopants is shown in Figs. 3a and b respectively. These results show that with increasing Cr or Mn content the solution energy of Sr becomes more favourable. More importantly, the mechanism by which this substitution reaction occurs remains that of oxygen vacancy formation. Similarly, the results for Fe and Cu show that oxygen vacancy formation was the most favourable mechanism of charge compensation. However, the trend for Cu contrasts with those predicted for Cr, Mn and Fe. To illustrate this difference, Fig. 4 displays the results for the Cu and Fe system *via* oxygen vacancy compensation only, which shows the contrasting effects of Fe and Cu doping. As

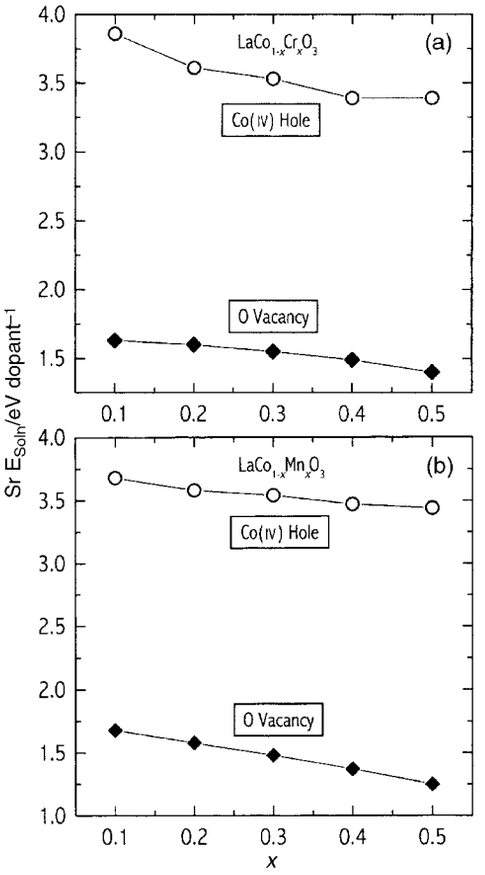

Fig. 3 Plot of Sr solution energy as a function of x: (a) $LaCo_{1-x}Cr_xO_3$, (b) $LaCo_{1-x}Mn_xO_3$.

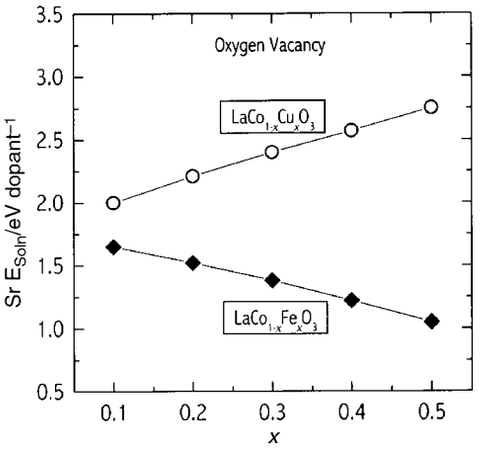

Fig. 4 Plot of Sr solution energy as a function of x for $LaCo_{1-x}M_xO_3$ (M = Fe, Cu) *via* oxygen vacancy compensation.

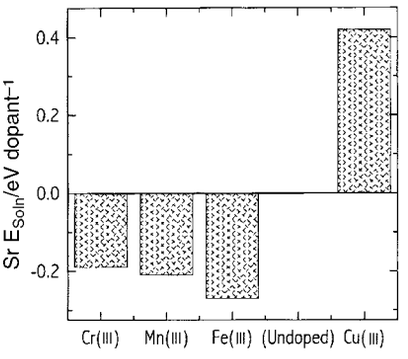

Fig. 5 Plot of Sr solution energy as a function of dopant M for $LaCo_{0.8}M_{0.2}O_3$ (M = Cr, Mn, Fe, Cu) *via* an oxygen vacancy mechanism and normalised to $LaCoO_3$ as the baseline.

the Cu and Fe level increases, the Sr solution energy decreases in the Fe system, but increases in the Cu system.

To highlight this trend further, Sr solution energies were calculated for a fixed composition $LaCo_{0.8}M_{0.2}O_3$ (M = Cr, Mn, Fe, Cu) relative to the undoped material and are presented in Fig. 5. It can be clearly seen that Cr, Mn and Fe doping lowers the Sr solution energy relative to undoped $LaCoO_3$ in the order Fe > Mn > Cr. Consequently for a given dopant concentration, Sr will dissolve most readily in the system containing Fe which will produce the oxygen vacancies required for H_2O_2 decomposition. In contrast, Cu doping increases the Sr solution energy which inhibits oxygen vacancy formation. The reaction model suggests that these oxygen vacancies increase the catalytic performance of these systems. However, the converse is predicted for Cu which would not break down the H_2O_2 oxidising agent to the same extent. These results correlate well with the observed catalytic performance which finds that the activity with regard to H_2O_2 decomposition is enhanced by Sr addition but suppressed by Cu.[35]

3.3 Surface energies and crystal morphology

This part of the study extends the scope of the bulk simulations by focusing on the surface structure of $LaCoO_3$ and the examination of the relevant defects at different surfaces. Limited attention has been paid to the structure and defect chemistry of the $LaCoO_3$ surfaces. To our knowledge, these are the first detailed simulations of the surfaces of the $LaCoO_3$ perovskite.

The interatomic potentials used in this surface work were directly transferred from the study of the bulk phase. Their application to surfaces assumes that the charge and polarisability of the surface ions is essentially that of the bulk. Surface studies of α-Al_2O_3 and MgO have compared quantum mechanical (QM) calculations with potential model simulations and found good agreement with the two methods.[65,66] The QM results also show that the ionicity at the surface is very similar to the bulk affirming the validity of using bulk potentials to model oxide surfaces.

We have focused our attention on the low index surfaces of cubic $LaCoO_3$, namely {100}, {110} and {111}. Cleavage of these three planes leads to two different dipolar surfaces or 'Type III' surfaces for each Miller index and hence all the surfaces will have divergent surface energies in the macroscopic limit. The dipole and its associated divergent energy can be removed by surface reconstruction. As described earlier the simplest reconstruction involves transferring half the ions from one surface to the complementary surfaces, as shown in Fig. 6.

Surface energies were calculated for each reconstructed surface using a sufficiently large region size ensuring the energies had converged and were independent of crystal size.

The calculated unrelaxed and relaxed surface energies for the three surfaces of $LaCoO_3$ are reported in Table 2. Considerable relaxation occurs (up to 76% reduction in the surface energy) suggesting that the relaxation of ions in the surface region can significantly increase the stability of the surface. From the relaxed surface energies listed in Table 2, it is predicted that the {100} and {111} surfaces will terminate with La and O ions, and the {110} surface with an oxide layer.

The results for $LaCoO_3$ are similar to simulations on the $SrTiO_3$ perovskite[67] where lattice relaxation contributes to the final structure and energy of the surfaces, but does not change the order of the surface energies. It is clearly seen that the order of stability for the relaxed surfaces of undoped $LaCoO_3$ is:

$$\{110\} > \{100\} > \{111\}$$

Experimental surface energies, which are difficult to measure,

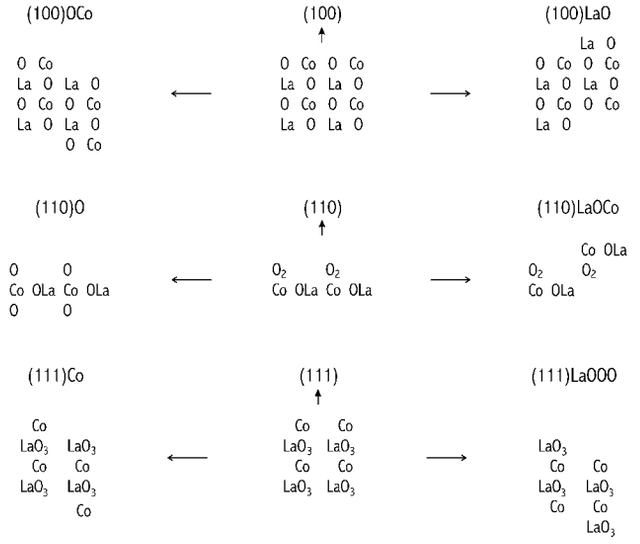

Fig. 6 Schematic representations of the surfaces of $LaCoO_3$ and the reconstruction technique employed to cancel the dipole of these type III surfaces.

are unavailable for $LaCoO_3$. Nevertheless, the energies presented here are in the range obtained from previous simulations of the $SrSnO_3$ perovskite[68] and other oxide systems.[52,53,69] On examination of these relaxed surfaces it is clear that reconstructions which preserve or generate intact CoO_6 octahedra are the most stable. This trend is also observed in the $SrSnO_3$ perovskite[68] where the {110} (O-terminating) surface is predicted to be the most stable. $SrSnO_3$ is however subject to complex orthorhombic distortions which tilt the SnO_6 octahedra causing differences in surfaces which are equivalent in the cubic perovskite.

The predicted contribution of the surfaces to the crystal morphology of $LaCoO_3$ is shown in Table 3. Schematic representations of the single crystal shapes are shown in Fig. 7 indicating a hexagonal-type habit. Although there are limited data on pure $LaCoO_3$ for direct comparison, the calculated morphology is consistent with SEM studies of $LaFeO_3$[70] and TEM studies of $LaCo_{0.8}Cu_{0.2}O_3$[71] which show almost regular hexagonal prismatic crystals. Examination of the results shows that if the surfaces are not relaxed, only the {110} surface will be observed in the morphology. However, on relaxation, a significant contribution is made from the {100} surface which alters the morphology. The results therefore suggest that the {110} and {100} surfaces are expected to play an important role both in catalysis and in surface oxygen exchange for electrochemical applications.

3.4 Surface structures of $LaCoO_3$

The relaxed structures of the most favourable low-index planes of $LaCoO_3$ have been calculated and are discussed in the following subsections.

3.4.1 {100} Surface. A cross-sectional view of the {100} surface is shown in Fig. 8. The top row of atoms represents those lying at the outermost surface in the {100} plane. Subsequent layers of atoms underneath these descend into the bulk of the crystal to a depth of $\approx$10 Å. Figs. 6 and 8 both show how this surface has been reconstructed to terminate with La and O ions. Fig. 8 shows that insignificant displacement of the La ions occurs on relaxation of the surface. However, in order to reduce the surface energy and strain, the Co and O ions of CoO_6 and CoO_5 units at the surface rearrange themselves extensively. Oxygen ions directly underneath the surface La are displaced (1.6 Å) from the Co–O layer to the outer La–O layer. These relaxations cause a sinusoidal displacement of the Co–O planes, both perpendicular and parallel to the surface, which diminishes until negligible displacements occur some 35 Å into the bulk. This surface rearrangement effects a dramatic reduction of the surface energy by 76%.

Table 2 Calculated surface energies of $LaCoO_3$

	Surface energy/J m^{-2}	
Miller index[a]	Unrelaxed	Relaxed
(100)OCo	6.62	2.68
(100)LaO	9.04	2.18
(110)O	5.50	2.05
(110)LaOCo	10.30	3.87
(111)Co	8.27	3.72
(111)LaOOO	10.25	3.11

[a]Terminating ions are indicated (see Fig. 6).

Table 3 Predicted morphology for $LaCoO_3$

	Unrelaxed		Relaxed	
Surface	Surface energy /J m^{-2}	% Area	Surface energy /J m^{-2}	% Area
100	9.04	0.0	2.18	17.2
110	5.50	100.0	2.05	82.8
111	10.25	0.0	3.11	0.0

3.4.2 {110} Surface. Fig. 9 shows the {110} surface in cross-section and how this surface has been reconstructed to terminate with an oxide layer. It is found that minimal

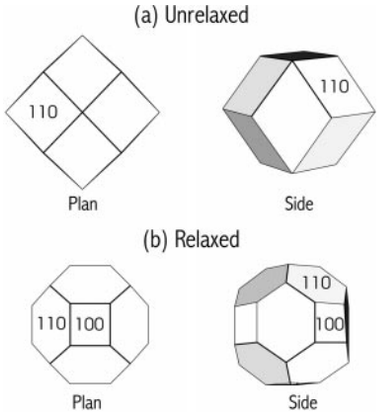

Fig. 7 Schematic showing the predicted crystal morphology of $LaCoO_3$ (plan and side views): (a) unrelaxed, (b) relaxed.

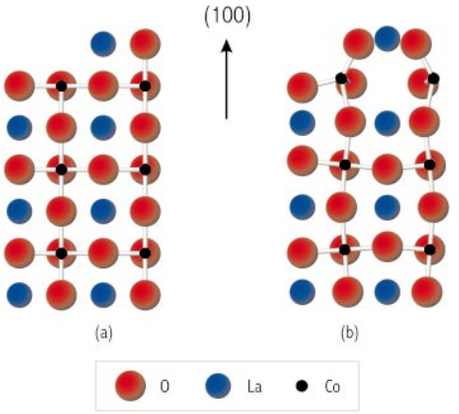

Fig. 8 The unrelaxed (a) and relaxed (b) surface structure (side views) for the {100} surface of $LaCoO_3$.

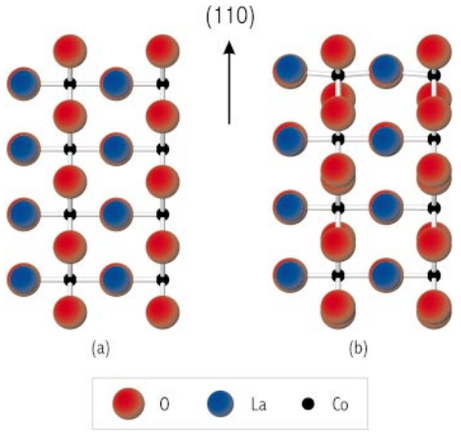

Fig. 9 The unrelaxed (a) and relaxed (b) surface structure (side views) for the {110} surface of $LaCoO_3$.

displacement of the La ions occurs on relaxation of the surface. The surface energy is reduced *via* the CoO_6 octahedra tilting about their axis perpendicular to the surface plane. This causes the outermost surface oxygen ions to relax towards the bulk (by 0.5 Å). This relaxation also causes the surface layers to rumple, a rearrangement which reduces the surface energy by 63%.

3.4.3 {111} Surface. Fig. 10 depicts the cross-sectional view of the reconstructed {111} surface which terminates with La and O ions. The surface CoO_6 octahedra have rearranged quite extensively in order to reduce the surface energy. Both La and O ions at the surface relax away from the bulk ($\approx$0.3 Å). This relaxation causes sinusoidal displacements in both axial and equatorial Co–O planes which become negligible after a depth of 25 Å into the bulk structure.

Figs. 8 and 10 show how the {111} surface relaxes to form lanthanum oxide 'ridges' at the surface which is also rumpled. Rumpling also occurs on the other two surfaces in common with those comprising more than one type of ion.[67]

3.5 Defects and dopants at surfaces

The overall relaxed structure involves predominantly oxygen terminated surfaces but includes some exposed lanthanum from the {100} surfaces. Our simulations of the bulk crystal indicate that these oxygen sites are important since Sr doping leads to oxygen vacancies.

We now extend our defect simulations to the low index surfaces of $LaCoO_3$, where we have calculated the energies of single point defects and neutral defect clusters on the relaxed surfaces. The initial starting point was the pure relaxed surface

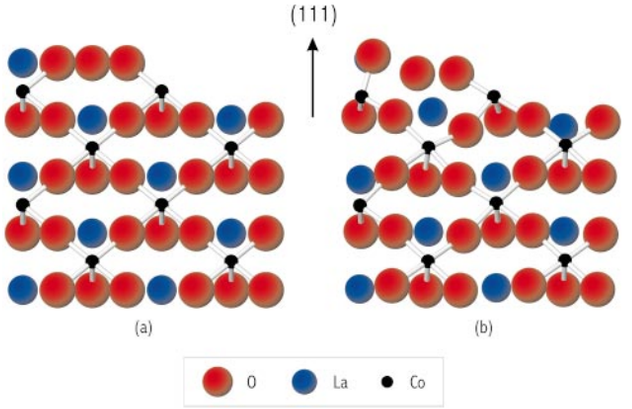

Fig. 10 The unrelaxed (a) and relaxed (b) surface structure (side views) for the {111} surface of $LaCoO_3$.

Table 4 Sr solution energies (eV per dopant) at the $LaCoO_3$ surfaces for the three compensation mechanisms (bulk values included for comparison)

Mechanism	100	110	111	Bulk
$h^{\cdot}_{Co_{(IV)}}$	3.21	2.80	2.57	2.42
$h^{\cdot}_{O_{(I)}}$	4.05	2.93	3.53	6.11
$V^{\cdot\cdot}_{O}$	1.50	1.13	1.53	1.79

obtained from the perfect surface calculations. Various geometries exist for the defect clusters, *i.e.* at each surface there are several sites in which the oxygen vacancy and the Sr substitutional can be placed. Each possibility was examined, and the overall solution energies compared, with the lowest energy arrangement selected. Hence, in conjunction with the cohesive energy terms, the solution energies for Sr incorporation are calculated using eqn. (5) and (6). These are summarised in Table 4.

The results indicate that for the oxygen vacancy defect clusters, the energies are more favourable on the less stable surfaces and still lower in energy than the hole species. Furthermore, with the exception of Co(IV) formation, the solution energy of Sr is lower than in the bulk, which indicates favourable segregation of these defects to these surfaces. This phenomenon is also consistent with behaviour seen in related oxides including CeO_2[72] and $La_{2-x}Sr_xCuO_4$.[73] It is interesting to note that the oxygen hole energy decreases significantly from the bulk to the surface (Table 4). For both {100} and {110} the difference in energy between Co^{4+} and O^- holes is small, particularly in relation to the approximations made in evaluating the hole energies, so that holes of both types might exist (at higher oxygen partial pressure). Such O^- species, as well as peroxide and superoxide ions, have been suggested as possible active centres in the catalytic behaviour of perovskites. This is a topic for further study.

The prediction that oxygen vacancies will preferentially form at the surface of $LaCoO_3$ (as well as in the bulk) is an important result as these defect species are key sites in the decomposition of H_2O_2. Furthermore, it is interesting to note that experimental studies strongly suggest that oxygen ion vacancies play a key role in the reaction kinetics of methane combustion.[5] Oxygen vacancies at the surface of the catalyst are believed to act as active sites for the adsorption of oxygen and incorporation into the lattice. From the catalytic viewpoint, the {110} and {100} surfaces are predicted to dominate the equilibrium morphology. Moreover, Sr substitution is favourable at all surfaces, having a lower solution energy than in the crystal bulk. From recent work of Teraoka *et al.*, the active site for NO decomposition over doped $LaCoO_3$ is proposed to be the oxide ion vacancy.[34] As NO decomposition is a bimolecular reaction, the vacancies that adsorb and activate one NO molecule should be adjacent, in a so called "pair-site" model. The {100} has been suggested as a possible surface for this vacancy pair,[34] purely on the supposition that this surface terminates with oxygen ions that can form these 'pair-clusters'. Our simulations which show the {110} surface to be the most stable for $LaCoO_3$ may be significant since this surface terminates with an oxide layer enabling oxygen vacancies to form in close proximity to one another.

4 Conclusions

Atomistic simulation techniques have been used to investigate the defect and surface properties of the $LaCoO_3$ perovskite which are of relevance to applications in catalysis, fuel cells and ceramic membranes. The discussion has highlighted the following points:

(1) Cation substitution of the La site by alkaline earth metals show that the most soluble dopants are predicted to be

Sr^{2+} and Ca^{2+}, with the formation of oxygen vacancies and Co(IV). Oxygen ion vacancies within the $LaCoO_3$ lattice are believed to be key sites with regard to catalytic activity and to surface oxygen exchange. Sr doping of $LaCo_{1-x}M_xO_3$ (M^{3+} = Cr, Mn, Fe, Cu) also leads to oxygen vacancy formation. This process is more favourable in the Fe system than in the Cu system. These results are in accord with the observed catalytic performance which found that activity towards H_2O_2 decomposition is enhanced by Sr addition but suppressed by Cu.

(2) Relaxed surface energies were calculated for low index surfaces of $LaCoO_3$ with the order of stability found to be: {110} > {100} > {111}. The calculations highlight the importance of modelling the relaxation at oxide surfaces, which confirms that deductions of catalytic activity based on ideal (unrelaxed) surfaces may be flawed. There are currently limited experimental data with which comparisons may be made. Indeed, one of the aims of this study is to encourage further experimental work using surface sensitive techniques (*e.g.* LEED, STM or HREM).

(3) The equilibrium morphology of the single crystal is predicted to be hexagonal-like. Simulations predict that the {110} surface will dominate the low-temperature crystal morphology in the absence of impurities, water or surface irregularities, with a lesser contribution from the {100} surface.

(4) Sr doping at the surface leads to the formation of oxygen vacancies which is consistent with bulk predictions and with models in which oxygen vacancies are thought to play a key catalytic role. The defect energies at the surface are generally lower than in the bulk crystal. This suggests the segregation of Sr dopant ions and oxygen vacancies to the surfaces, which is important for catalytic activity and surface oxygen exchange.

Acknowledgements

This work was supported by a EPSRC/CASE studentship with Synetix (M.S.D.R.). We wish to thank Prof. S. C. Parker and Dr. J. D. Gale for helpful discussions. The simulations were performed on the supercomputer facilities at the Rutherford Appleton Laboratory.

References

1 L. G. Tejuca, J. L. G. Fierro and J. M. D. Tascon, *Adv. Catal.*, 1989, **36**, 237.
2 R. Lago, G. Bini, M. A. Pena and J. L. G. Fierro, *J. Catal.*, 1997, **167**, 198.
3 N. Yamazoe and Y. Teraoka, *Catal. Today*, 1990, **8**, 175.
4 Y. Teraoka, H. Nii, S. Kagawa, K. Jansson and M. Nygren, *J. Mater. Chem.*, 1996, **6**, 97.
5 J. G. McCarty and H. Wise, *Catal. Today*, 1990, **8**, 231.
6 T. Tagawa and H. Imai, *J. Chem. Soc., Faraday Trans.*, 1988, **84**, 923.
7 K. Omata, O. Yamazaki, K. Tomita and K. Fujimoto, *J. Chem. Soc., Chem. Commun.*, 1994, **14**, 1647.
8 C. B. Alcock, J. J. Carberry, R. Doshi and N. Gunasekaran, *J. Catal.*, 1993, **143**, 533.
9 J. E. ten Elshof, H. J. M. Bouwmeester and H. Verweij, *Appl. Catal. A*, 1995, **130**, 195.
10 T. Hayakawa, H. Orita, M. Shimizu, K. Takehira, A. G. Andersen, K. Nomura and Y. Ujihira, *Catal. Lett.*, 1992, **16**, 359.
11 K. S. Chan, J. Ma, S. Jaenicke, G. K. Chuah and J. Y. Lee, *Appl. Catal. A*, 1994, **107**, 201.
12 P. D. Petrolekas and I. S. Metcalfe, *J. Catal.*, 1995, **152**, 147.
13 N. Mizuno, M. Tanaka and M. Misono, *J. Chem. Soc., Faraday Trans.*, 1992, **88**, 91.
14 A. Lindstedt, D. Stromberg and M. A. Milh, *Appl. Catal. A*, 1994, **116**, 109.
15 L. Lisi, G. Bagnasco, P. Ciambelli, S. De Rossi, P. Porta, G. Russo and M. Turco, *J. Solid State Chem.*, 1999, **146**, 176.
16 C. Oliva, L. Forni, P. Pasqualin, A. D'Ambrosio and A. V. Vishniakov, *Phys. Chem. Chem. Phys.*, 1999, **1**, 355.
17 N. M. Sammes and B. C. H. Steel, *J. Catal.*, 1994, **145**, 187.
18 M. Stojanovic, R. G. Haverkamp, C. A. Mims, H. Moudallal and A. J. Jacobsen, *J. Catal.*, 1997, **166**, 315.
19 J. Kirchnerova, D. Klvana, J. Vaillancourt and J. Chaouki, *Catal. Lett.*, 1993, **21**, 77.
20 V. R. Choudhary, B. S. Uphade, S. G. Pataskar and G. A. Thite, *Chem. Commun.*, 1996, 1021.
21 S. T. Aruna, M. Muthuraman and K. C. Patil, *J. Mater. Chem.*, 1997, **7**, 2499.
22 A. Baiker, P. E. Marti, P. Keusch, E. Fritsch and A. Reller, *J. Catal.*, 1994, **146**, 268.
23 W. Schäfer, A. Kock, U. Herold-Schmidt and D. Stolten, *Solid State Ionics*, 1996, **86–88**, 1235.
24 V. V. Kharton, A. V. Kovalevsky, V. N. Tikhonovich, E. N. Naumovich and A. P. Viskup, *Solid State Ionics*, 1998, **110**, 53.
25 B. C. H. Steele, *Solid State Ionics*, 1996, **86–88**, 1223.
26 N. Q. Minh, *J. Am. Chem. Soc.*, 1993, **76**, 563.
27 H. U. Anderson, *Solid State Ionics*, 1992, **52**, 33.
28 T. Ishigaki, S. Yamauchi, K. Kishio, J. Mizusaki and K. Fueki, *J. Solid State Chem.*, 1988, **73**, 179.
29 R. A. De Souza and J. A. Kilner, *Solid State Ionics*, 1999, **126**, 153.
30 J. A. Lane, S. J. Benson, D. Waller and J. A. Kilner, *Solid State Ionics*, 1999, **121**, 201.
31 A. Belzner, T. M. Gür and R. A. Huggins, *Solid State Ionics*, 1992, **57**, 327.
32 H. J. M. Bouwmeester, H. Kruidhof, A. J. Burggraaf and P. J. Gellings, *Solid State Ionics*, 1992, **53–56**, 460.
33 R. H. E. van Doorn, H. J. M. Bouwmeester and A. J. Burggraaf, *Solid State Ionics*, 1998, **111**, 263.
34 Y. Teraoka, T. Harada and S. Kagawa, *J. Chem. Soc., Faraday Trans.*, 1998, **94**, 1887.
35 J. Hollingworth, W. R. Flavell, A. G. Thomas, S. C. Grice, C. E. J. Mitchell, P. M. Dunwoody, S. Warren, S. J. Squire, P. G. D. Marr, S. W. Downes and F. E. Hancock, *J. Electron Spectrosc. Relat. Phenom.*, 1999, **103**, 765.
36 M. S. D. Read, M. S. Islam, F. King and F. E. Hancock, *J. Phys. Chem. B*, 1999, **103**, 1558.
37 D. J. Ilett and M. S. Islam, *J. Chem. Soc., Faraday Trans.*, 1993, **89**, 3833.
38 M. S. Islam, M. Cherry and L. J. Winch, *J. Chem. Soc., Faraday Trans.*, 1996, **92**, 479.
39 J. D. Gale, *J. Chem. Soc., Faraday Trans.*, 1997, **93**, 629.
40 G. W. Watson, E. T. Kelsey, N. H. de Leeuw, D. J. Harris and S. C. Parker, *J. Chem. Soc., Faraday Trans.*, 1996, **92**, 433.
41 P. W. Tasker, *Philos. Mag. A*, 1979, **39**, 119.
42 *Solids State Chemistry: Techniques*, ed. A. K. Cheetham and P. Day, Clarendon Press, Oxford, 1987.
43 D. E. Parry, *Surf. Sci.*, 1975, **49**, 433; D. E. Parry, *Surf. Sci.*, 1976, **54**, 195.
44 P. P. Ewald, *Ann. Physik.*, 1921, **64**, 253.
45 M. Cherry, M. S. Islam and C. R. A. Catlow, *J. Solid State Chem.*, 1995, **118**, 125.
46 J. H. Harding, *Rep. Prog. Phys.*, 1990, **53**, 1403.
47 F. Bertaut, *Compt. Rendu.*, 1958, **246**, 3447.
48 P. W. Tasker, *J. Phys. C: Solid State Phys.*, 1979, **12**, 4977.
49 P. M. Oliver, S. C. Parker and W. C. Mackrodt, *Modelling Simul. Mater. Sci. Eng.*, 1993, **1**, 755.
50 G. Wulff, *Z. Kristallogr. Kristallgeom.*, 1901, **39**, 449.
51 J. W. Gibbs, *On the Equilibrium of Heterogeneous Substances*, Longman, New York, 1st edition, 1928.
52 P. M. Oliver, G. W. Watson, E. T. Kelsey and S. C. Parker, *J. Mater. Chem.*, 1997, **7**, 563.
53 S. C. Parker, P. M. Oliver, N. H. DeLeeuw, J. O. Titiloye and G. W. Watson, *Phase Transitions*, 1996, **61**, 83.
54 M. J. Davies, S. C. Parker and G. W. Watson, *J. Mater. Chem.*, 1994, **4**, 813.
55 G. V. Lewis and C. R. A. Catlow, *J. Phys. C: Solid State Phys.*, 1985, **18**, 1149.
56 M. S. Khan, M. S. Islam and D. R. Bates, *J. Phys. Chem. B*, 1998, **102**, 3099.
57 M. S. Islam, *J. Mater. Chem.*, 2000, **10**, 1027.
58 F. King and F. E. Hancock, unpublished work.
59 Y. Teraoka, M. Yoshimatsu, N. Yamazoe and T. Seiyama, *Chem. Lett.*, 1984, 893.
60 Z. Yu, L. Gao, S. Yuan and Y. Wu, *J. Chem. Soc., Faraday Trans.*, 1992, **88**, 3245.
61 G. Balducci, J. Kašpar, P. Fornasiero, M. Graziani and M. S. Islam, *J. Phys. Chem. B*, 1997, **101**, 1750.
62 G. Balducci, J. Kašpar, P. Fornasiero, M. Graziani, M. S. Islam and J. D. Gale, *J. Phys. Chem. B*, 1998, **102**, 557.

63 B. Ammundsen, J. Roziere and M. S. Islam, *J. Phys. Chem. B*, 1997, **101**, 8156.
64 M. S. Khan, M. S. Islam and D. R. Bates, *J. Mater. Chem.*, 1998, **8**, 2299.
65 I. Manassidis and M. J. Gillan, *J. Am. Ceram. Soc.*, 1994, **77**, 335.
66 W. C. Mackrodt and P. W. Tasker, *J. Am. Ceram. Soc.*, 1989, **72**, 1576.
67 W. C. Mackrodt, *J. Chem. Soc., Faraday Trans.*, 1989, **85**, 541.
68 R. I. Hines, N. L. Allan and W. R. Flavell, *J. Chem. Soc., Faraday Trans.*, 1996, **92**, 2057.
69 M. S. Islam, D. J. Ilett and S. C. Parker, *J. Phys. Chem.*, 1994, **98**, 9637.
70 E. Traversa, P. Nunziante, M. Sakamoto, Y. Sadaoka, M. C. Carotta and G. Martinelli, *J. Mater. Res.*, 1998, **13**, 1335.
71 P. Porta, S. De Rossi, M. Faticanti, G. Minelli, I. Pettiti, L. Lisi and M. Turco, *J. Solid State Chem.*, 1999, **146**, 291.
72 T. X. T. Sayle, S. C. Parker and C. R. A. Catlow, *J. Phys. Chem.*, 1994, **98**, 13625.
73 P. R. Kenway, S. C. Parker and W. C. Mackrodt, *Surf. Sci.*, 1995, **326**, 301.
74 R. C. Baetzold and M. S. Islam, unpublished work..